SCIENCE CHINA
Life Sciences

•RESEARCH PAPER•

June 2021 Vol.64 No.6: 966–981
https://doi.org/10.1007/s11427-020-1762-2

Proteome landscape and spatial map of mouse primordial germ cells

Pan Wang[1], Yilong Miao[2], Xiao-Han Li[2], Na Zhang[1,3,4], Qilong Wang[1,3,4], Wei Yue[1,3,4], Shao-Chen Sun[2], Bo Xiong[2*], Jie Qiao[1,3,4] & Mo Li[1,3,4*]

[1]*Center for Reproductive Medicine, Peking University Third Hospital, Beijing 100191, China;*
[2]*College of Animal Science and Technology, Nanjing Agricultural University, Nanjing 210095, China;*
[3]*National Clinical Research Center for Obstetrics and Gynecology, Beijing 100191, China;*
[4]*Key Laboratory of Assisted Reproduction (Peking University), Ministry of Education, Beijing 100191, China*

Received April 6, 2020; accepted June 19, 2020; published online August 26, 2020

Primordial germ cells (PGCs) are precursors of both male and female gametes as fundamental materials for organism development. The transcriptome, methylome, and chromatin accessibility profiles of PGCs in both mice and humans have been recently reported. However, little is known about the characteristics of PGCs at the protein levels, which directly exert cellular functions. Here, we construct landscapes of both proteome and 3D spatial distribution of mouse PGCs at E11.5, E13.5 and E16.5 days, the three critical developmental windows for PGCs' sex differentiation, female meiosis initiation and male mitotic arrest. In each developmental stage of PGCs, nearly 2,000–3,000 proteins are identified, among which specific functional pathways such as oxidative phosphorylation, DNA damage repair, and meiotic cell cycle are involved for different events during PGCs development. Interestingly, by 3D modeling we find that PGCs spatially cluster into around 1,300 nests in genital ridge at E11.5 and the nest number is not increased by the exponential proliferation of PGCs. Comparative analysis of our proteomic data with published transcriptomic data does not show a close correlation, meaning that the practically executive factors are beyond the transcriptome. Thus, our work offers a valuable resource for the systematic investigations of PGC development at protein level and spatial map.

PGCs, proteome, spatial map, sex differentiation, meiosis

Citation: Wang, P., Miao, Y., Li, X.H., Zhang, N., Wang, Q., Yue, W., Sun, S.C., Xiong, B., Qiao, J., and Li, M. (2021). Proteome landscape and spatial map of mouse primordial germ cells. Sci China Life Sci 64, 966–981. https://doi.org/10.1007/s11427-020-1762-2

INTRODUCTION

In organisms with sexual reproduction, primordial germ cells (PGCs) are embryonic precursors of sperm and egg that pass on genetic and epigenetic information to subsequent generations (Ewen and Koopman, 2010; Hayashi et al., 2007). PGC specification in mammals involves a series of key molecular and cellular events that turn off the somatic program and switch on the germline program to separate the germline from the somatic lineages (Martínez-Arroyo et al., 2014). In mouse model, PGCs derive from a small group of proximal epiblast cells and become identifiable as alkaline phosphatase (AP)- and Prdm1-positive cells at the base of the incipient allantois in the extraembryonic mesoderm at around embryonic day (E) 7.25 (Saitou and Yamaji, 2010). During gastrulation, PGCs migrate to the developing hindgut endoderm at E7.75, into the mesentery at E9.5, and colonize the genital ridges at around E10.5. After that, PGCs initiate their sexual determination guided by the surrounding mi-

*Corresponding authors (Mo Li, email: limo@hsc.pku.edu.cn; Bo Xiong, email: xiongbo@njau.edu.cn)

croenvironment of the gonadal niche. From about E13.5, male germ cells enter the mitotic arrest until the neonatal stage, then resume mitotic proliferation soon after birth, and subsequently enter meiosis during puberty. In the meantime, female PGCs enter the meiotic prophase and arrest at the diplotene stage, followed by the resumption of meiosis by hormonal stimulation during adulthood (Saitou and Yamaji, 2012; Tan and Tee, 2019). The molecular basis and network of PGC differentiation and development are largely unknown.

Infertility is a common clinical problem which affects 13% to 15% of couples worldwide (Agarwal et al., 2015). Associated factors for infertility are complicated and the treatment usually does not result in a desired birth outcome especially when the gametes are not functional (Wen et al., 2020). Increasing evidence shows that errors in PGCs meiotic progress including chromosomal recombination, synapsis, and chiasmata formation are one of major causes for the failure of germ cell development and infertility (Bhattacharyya et al., 2019; Paigen and Petkov, 2010). With the advance of stem cell biology, PGCs can be obtained from pluripotent stem cells (Hikabe et al., 2016), thus providing a new therapeutic possibility to treat infertile couples. Recent studies of the transcriptome, epigenome, and chromatin accessibility analysis have dramatically extended our understanding of genetic and epigenetic network regulating the PGC development (Guo et al., 2017; Seisenberger et al., 2012; Yamaguchi et al., 2013). However, proteins act as the executors of most biological processes and their abundance cannot be directly predicted from the transcripts. Therefore, the proteome data allow us to identify the core factors and signaling pathways orchestrating key events in PGC differentiation and development, thereby offering a valuable resource for further mechanistic studies and applications.

In the present study, we profile PGC proteome at crucial development stages combined with reconstructing a 3D map of PGCs in intact genital ridge. Nearly 2,000–3,000 proteins are identified in different stages of PGCs, in which distinct functional pathways are involved for each stage. Oxidative phosphorylation, fatty acid oxidation and electron transport chain are found activated during the female and male PGC differentiation processes, while ATM signaling pathway and synapsis are activated for female PGCs at meiosis prophase I. Taking advantage of tissue volume multiplex imaging, we display a 3D panorama of spatial distribution of mouse PGCs *in situ*. PGCs cluster into around 1,300 nests in genital ridge at E11.5 and the nest number is not increased by the exponential proliferation of PGCs. Comparative analysis of our proteomic data with published transcriptomic data does not show a close correlation, indicating a gap or expression delay between these executive factors and the transcriptome. Collectively, this study provides a valuable functional resource of PGCs at levels of protein and *in site* space.

RESULTS

Spatial map of PGC

To visualize PGCs *in situ*, we employed Oct4-GFP transgenic mice in which the GFP protein is fused with Oct4, a representative expressing marker for PGCs (Sabour et al., 2011; Seisenberger et al., 2012) (Figure S1 in Supporting Information). At E11.5 before sex differentiation, Oct4 expression was relatively weak in the genital ridge, indicating the lower number of PGCs at this stage. At E13.5, the expressions of Oct4 became stronger and comparable in the male and female gonads, although the female exhibited a spotty pattern whereas the male displayed a wavy pattern reflecting the testicular tubule formation. At E16.5, Oct4 expression persisted with similar patterns as E13.5 in the growing female and male gonads (Figure 1A).

Combining volume multiplex imaging (Li et al., 2019) with Imaris 3D modeling, we monitored the distribution dynamics and colonization pattern of PGCs in the genital ridge as well as differentiated male and female gonads in Oct4-GFP transgenic mice. Fluorescence-labeled PGCs were 3D-reconstructed in intact genital ridge. As shown in Figure 1B, PGCs clustered into foci (i.e., nests) rather than existed individually at the beginning of their colonization in the genital ridge (E11.5), which is consistent with the previous reports (Lei and Spradling, 2013; Pepling and Spradling, 2001). After sex differentiation, both female and male PGCs also existed in the nests form at E13.5 and E16.5. In assessing the nest number and volume, we found that although the number did not dramatically change during PGC differentiation, the nest volume underwent a significant increase (~8 fold) from E11.5 to E13.5, and a decrease (2–4 fold) from E13.5 to E16.5 (Figure 1C and D), meaning that until E13.5, PGCs keep the proliferation within the located nests, while after E13.5 when less proliferation occurs, the nests start to fragment. Quantitative measurement of the volume of genital ridge and gonads displayed that female gonads at E13.5 and E16.5 remained the comparable size as the genital ridge, whereas the male gonads grew up remarkably with the development (Figure 1E and F). These data provide a spatial panorama of PGCs and their proliferating pattern within the genital ridge and gonads.

Isolation of mouse PGCs

Although previous studies have reported the transcriptome profiles of mouse and human PGCs (Gkountela et al., 2013; Guo et al., 2015; Jameson et al., 2012), the developmental regulation of protein expression of PGCs is still unknown. To address this question, we firstly aimed to isolate PGCs at different time points during sex differentiation using Oct4-GFP transgenic mice. Fluorescence-activated cell sorting (FACS) was used to enrich Oct4-GFP positive PGCs at

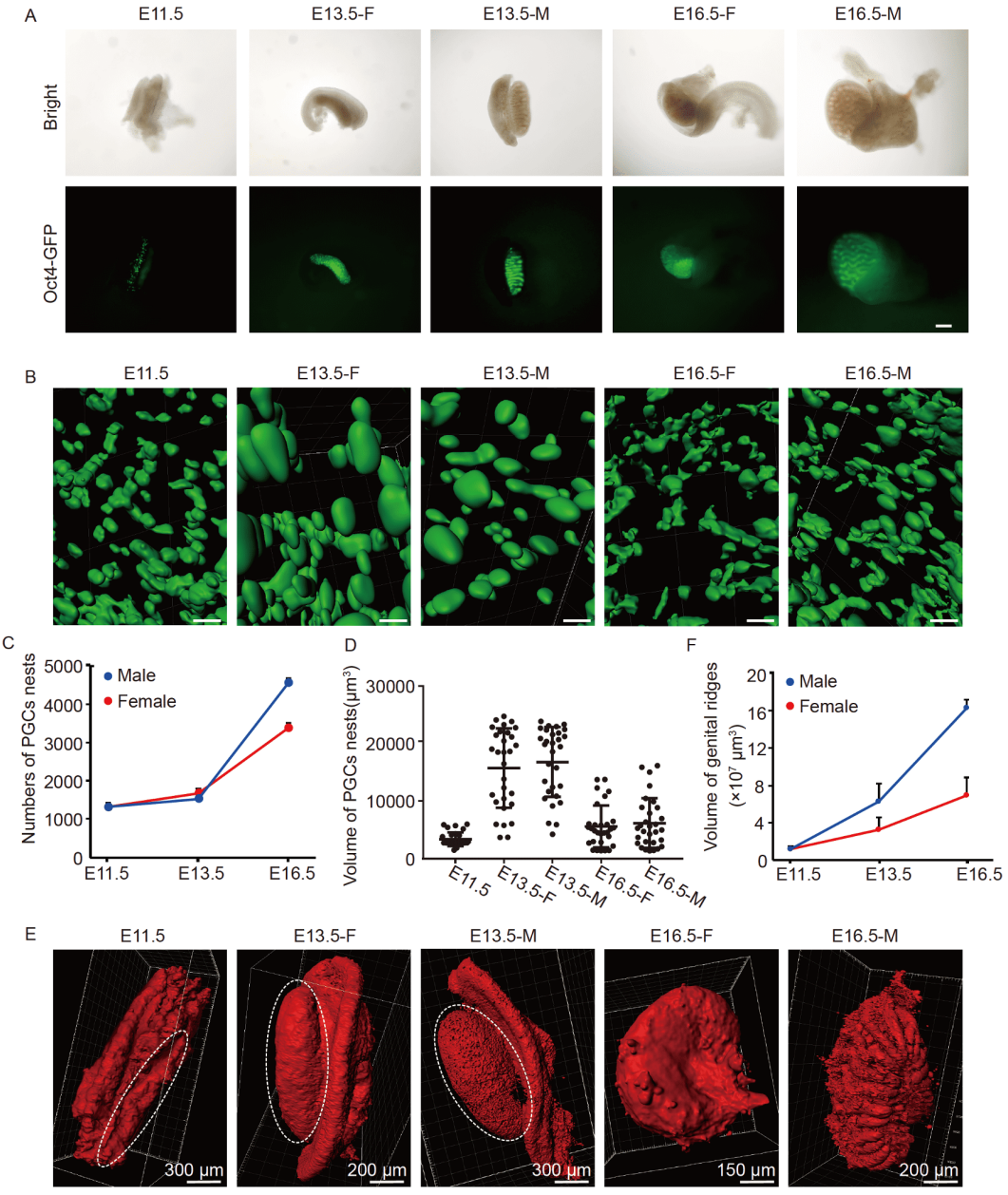

Figure 1 Spatial map of mouse PGCs in intact genital ridges. A, Fluorescent imaging of PGCs in intact genital ridges at different stages. Intact genital ridges at E11.5 (with mesonephros), E13.5 (with mesonephros), and E16.5 were surgically isolated from pregnant Oct4-GFP transgenic mice followed by whole tissue fluorescent imaging. PGCs were marked by Oct4-GFP. Scale bar, 200 μm. B, 3D construction of PGC nests in intact genital ridges at different stages. Intact genital ridges were volume imaged and the fluorescent PGC nests were *in situ* 3D-reconstructed by Imaris Surfaces. Scale bar, 30 μm. C, Number dynamics of PGC nests in mouse genital ridges at different stages. The number counting was conducted by Imaris Spots module. At least three genital ridges were included for each group. Error bars represent the standard deviation. D, Volume calculation of individual PGC nest in mouse genital ridges at different stages. Volume calculation was conducted by Imaris Surfaces Statistics. Thirty nests in genital ridges were included for each stage. Error bars represent the standard deviation. E, 3D modeling of intact genital ridges at different stages. Intact genital ridges at E11.5 (with mesonephros), E13.5 (with mesonephros), and E16.5 were surgically isolated from pregnant mice followed by tissue high-resolution scanning and Imaris Surfaces construction of somatic cells channel. The area of genital ridges at E11.5 and E13.5 was cycled by a dashed line. Scale bar, 200 μm. F, Volume calculation of intact genital ridges at different stages. The calculation was conducted by Imaris Surfaces Statistics. At least three genital ridges were included for each group. Error bars represent the standard deviation.

different stages (Figure 2A). An extra marker of PGCs, Vasa (Lin et al., 2008), was used for confirming these isolated PGCs (Figure 2B). Less than 1% of total cells in genital ridge were sorted as PGCs at E11.5. By contrast, the proportions of PGCs were increased to ~8% in both female and male gonads at E13.5 but decreased to ~4% in male gonads at E16.5 (Figure 2C). In specific, there were around 3,500 PGCs in E11.5 embryo, which is supported by early reports (Godin et al., 1990; Tam and Snow, 1981). This number increased to around 25,000 and 26,000 in E13.5 female and male em-

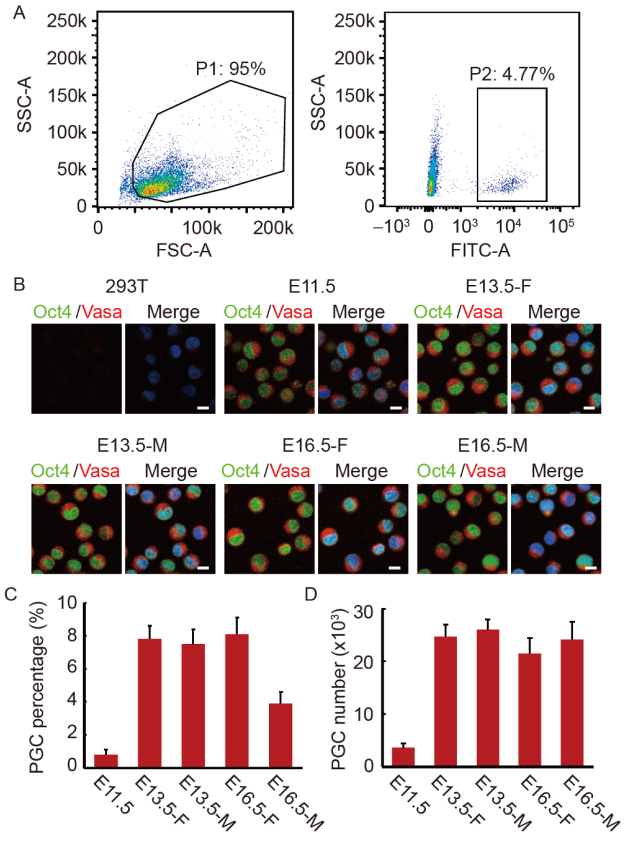

Figure 2 Isolation of mouse PGCs. A, Fluorescence-activated cell sorting (FACS) of mouse PGCs. The genital ridges at different stages were removed from pregnant Oct4-GFP transgenic mice followed by accutase digestion. GFP-positive cells were sorted using a FACS Aria II SORP cell sorter. B, Immunofluorescence staining of PGCs marker Vasa. The isolated cells by FACS were further stained with Vasa and DAPI to confirm the identity of PGCs. Scale bar, 10 μm. C, PGC rate in genital ridges at different stages. The ratio between PGCs and total cells in genital ridges were calculated. Cells from 10 genital ridges were used for each FACS. Three rounds of FACS were included for each group. Error bars represent the standard deviation. D, Number of PGCs in genital ridges at different stages. Cells from 10 genital ridges were used for each FACS and calculation. Three rounds of FACS were included for each group. Error bars represent the standard deviation.

bryos, respectively. Till E16.5, the PGC number did not significantly change (Figure 2D) as female PGCs enter meiosis and male PGCs stay arrest at mitosis.

Proteomic landscape of mouse PGCs

To gain insights into the key regulators and pathways during PGC differentiation, the protein profiles of PGCs at E11.5, E13.5 and E16.5 were acquired by performing LC-MS/MS combined with bioinformatics analysis. Sample density profile and violin plot showed that MS data and protein abundance followed the normal distribution in all samples (Figure S2A and B in Supporting Information). Principal component analysis (PCA) indicated that the biological replicates for each sample at different developmental stages displayed a high consistency (Figure 3A). E13.5 female and male PGCs clustered together and did not show a remarkable difference in protein profiling. However, E16.5 male PGCs separated far from the female PGCs, suggesting that PGCs exhibit the sex-biased changes in proteome after sex differentiation. Meanwhile, we found that PGCs at E11.5 were quite distinct from those at E13.5 and E16.5, implying that the sex differentiation of PGCs is initially established after E11.5 and before E13.5. These observations were further verified by the hierarchical clustering analysis (Figure 3B).

In addition, the Venn diagram showed that 1,950 proteins were detected in E11.5 PGCs, 2,477 proteins in E13.5 male PGCs, 2,843 proteins in E13.5 female PGCs, 2,867 proteins in E16.5 male PGCs and 3,008 female PGCs. Of them, 12 proteins were specifically expressed in E11.5 PGCs, 27 proteins were specifically expressed in E13.5 female PGCs, 8 proteins were specifically expressed in E13.5 male PGCs, 204 proteins were specifically expressed in E16.5 female PGCs, and 236 proteins were specifically expressed in E16.5 male PGCs (Figure 3C; Table S1 in Supporting Information). This indicates that with the differentiation and development, male and female PGCs start to express considerable unique proteins to prepare their subsequent development. Also, we performed a correlation analysis to compare our proteomic data with previously published transcriptomic data (Guo et al., 2017). Interestingly, the protein expression profiles during PGC differentiation and development were not closely correlated with the RNA expression profiles (Figure 3D). In general, the correlation coefficient of all three developmental windows was less than 0.43. The expression profiles between protein and RNA at E11.5 showed the lowest correlation. These results suggest that the transcriptome only represents an intermediate state of gene expression during PGC development which can reflect mechanisms such as transcriptional regulation and post-transcriptional regulation. By contrast, proteomic profiling provides information on real functional molecules and pathways.

Protein profiling during female PGC development

To further understand the core players regulating the female-biased differentiation process of PGCs, we comprehensively analyzed the protein expression profiles of female PGCs from E11.5 to E16.5 and found the prominent divergence at different developmental stages as shown by the heatmap of differentially expressed proteins (DEPs) and t-distributed stochastic neighbor embedding (t-SNE) analysis (Figure 4A; Figure S3A in Supporting Information). Functional annotation and gene ontology (GO) enrichment analysis of these DEPs were performed by WebGestalt (Figure 4B). Female DEPs at E13.5 were mainly responsible for the initiation of meiosis and epigenetic reprogramming events, such as "regulation of gene expression, epigenetic", "covalent chromatin modification", and "regulation of chromosome

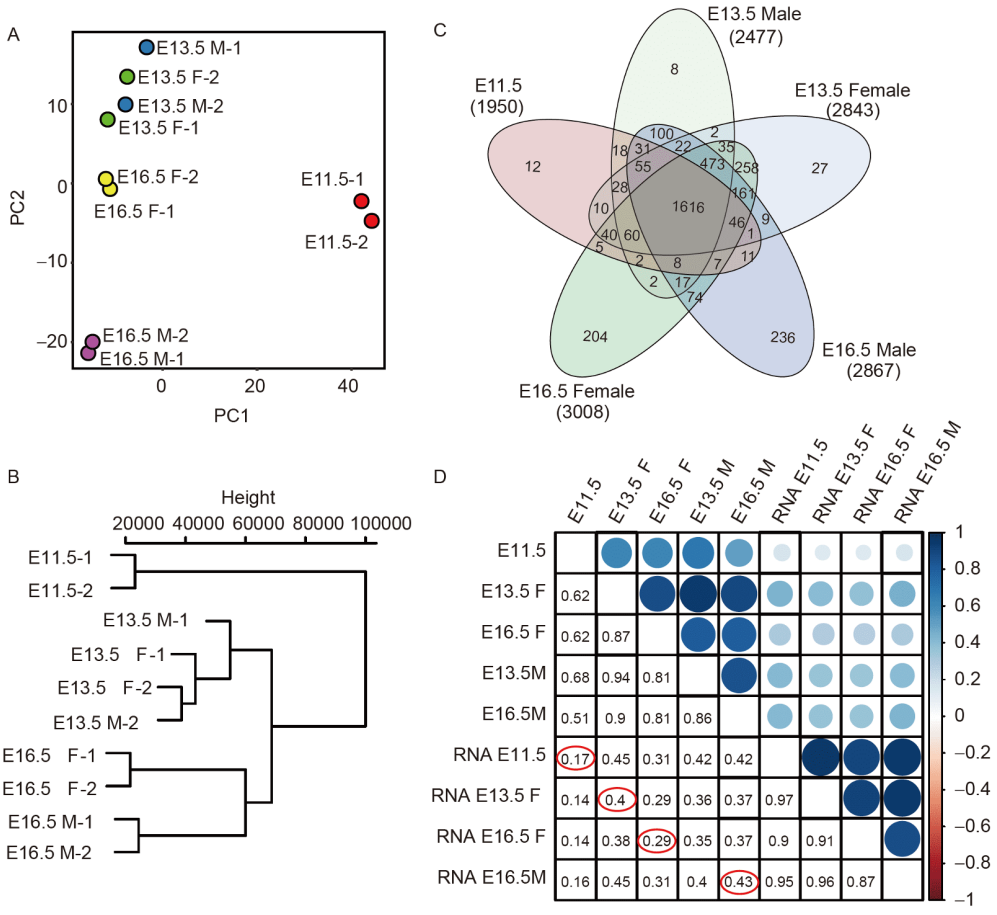

Figure 3 General proteomics analysis of mouse PGCs. A, Principal component analysis of PGCs proteome at different stages. Different colors represent PGCs at different stages. Two biological replicates were included for each stage. B, Hierarchical clustering of PGCs proteome at different stages. Multilevel hierarchy in the cluster tree shows similarity among PGCs proteome at different stages. C, Venn diagram analysis of PGCs proteome with differences and similarities among proteins identified at different stages. The total number and unique number of proteins identified for each stage are shown. D, Correlation between PGC proteome and transcriptome at different stages. Pearson correlation coefficient is visualized by color and size, and the corresponding values in the box. The values showing the correlations between proteome and transcriptome at the same stage are labeled in red.

organization". Also, this stage involved in the active protein synthesis by showing the GO terms of "regulation of cellular protein localization", "posttranscriptional regulation of gene expression", "protein acylation" and "translation initiation". While the most enriched category of DEPs in E16.5 female PGCs was "meiotic cell cycle", including the meiosis-specific proteins such as Dmc1, Hormad1, Hormad2, Meioc, Spata22, Tex12, and Ythdc2, which indicates their functions in the regulation and correct execution of meiosis at prophase I (Figure 4B). Furthermore, the GO terms "DNA recombination", "synaptonemal complex organization", "organelle fission", and "organelle fusion" suggest that these molecular events are active during female PGC development at E16.5 (Figure 4B).

Using fuzzy c-means algorithm, we clustered distinct protein expression profiles in female PGCs from E11.5 to E16.5. Clusters 2 and 5 represented the proteins that were upregulated from E11.5 to E16.5, clusters 1 and 6 represented proteins that were downregulated from E11.5 to E16.5, and clusters 3 and 4 depicted a bi-modal expression pattern that displayed increased expression at E13.5 but decreased expression at E16.5 (Figure 4C). GO analysis of clusters 2 and 5 showed that the upregulated proteins tend to exert functions in catabolic, metabolic, and cytosolic transport processes. The GO terms fell into the categories such as "ribose phosphate metabolic process", "tricarboxylic acid metabolic process", "cellular amino acid metabolic process" (cluster 2), and "Golgi vesicle transport" and "endosomal transport" (cluster 5), presumably providing materials and energy to support the PGC growth (sheet 2 and 5 in Table S2 in Supporting Information). Clusters 1 and 6 included the downregulated proteins in the process of RNA and nucleotide metabolism, including "RNA localization", "mRNA processing" (cluster 1) and "nucleotide phosphorylation", "nucleoside triphosphate metabolic process" (cluster 6), indicating that these molecular events occur in preparation for PGCs differentiation and the initiation of meiosis (sheet 1 and 6 in Table S2 in Supporting Information). Lastly, the proteins in clusters 3 and 4 were enriched in the processes of transcription and protein synthesis in E13.5 female PGCs,

such as "transcription by RNA polymerase I", "post-transcriptional regulation of gene expression", "translational initiation", "protein folding" (cluster 3), and "protein localization to chromosome" (cluster 4) (sheet 3 and 4 in Table S2 in Supporting Information).

Protein profiling during male PGC development

In parallel, we analyzed the protein expression profiles of male PGCs from E11.5 to E16.5 (Figure 4A). The heatmap of DEPs displayed sharp differences among E11.5, E13.5 and E16.5 male PGCs (Figure 4A), which was verified by t-SNE analysis showing that the protein profile clustering of PGCs at different developmental stages separated far from each other (Figure S3A in Supporting Information). These data indicate that developmental stage-specific protein expression is essential for male differentiation of PGCs and subsequent development. The GO biological process analysis by WebGestalt further showed the stage-specific functions exerted by these DEPs (Figure 4B). The data revealed that DEPs were enriched in the terms of "intermediate filament-based process", "skin development", "peptide cross-linking", and "regulation of binding" in E11.5 PGCs, indicating the colonization of PGCs at this stage. Whereas DEPs in E13.5 male PGCs were mainly enriched in RNA processing and many catabolic processes, such as "RNA localization", "RNA 3"-end processing", "ncRNA metabolic process", "cellular nitrogen compound catabolic process" and "aromatic compound catabolic process". In E16.5 male PGCs, "DNA modification" process functioned for the establishment of paternal imprints and *de novo* methyltransferases Dnmt3a and Dnmt3l were enriched in this protein set, contributing to the *de novo* methylation at this stage. The categories "methylation", "covalent chromatin modification", and "gene silencing" were consistent with the current notion about the epigenetic reprogramming and gene expression state in E16.5 male PGCs. While the term "negative regulation of organelle organization" displayed the entry of mitotic arrest (Figure 4B). These observations suggest that although male PGCs enter into the mitotic arrest and stay quiescent in the G0/G1 phase of the cell cycle for the remaining embryonic period upon entry into the genital ridge after E13.5, they already start to prepare the materials required for the spermatogenesis after birth.

In fuzzy c-means algorithm of males, six clusters of temporal patterns displaying different expression kinetics were identified (Figure 4C). Among them, clusters 1 and 6 represented the proteins that were up-regulated with the development, especially including those factors involved in the gene transcription, protein translation, as well as various metabolic and catabolic processes as shown by the GO enrichment analysis (sheet 1 and 6 in Table S3 in Supporting Information). By contrast, cluster 5 exhibited the down-regulation expression trend and contained many ribosomal proteins (sheet 5 in Table S3 in Supporting Information). Clusters 2, 3, and 4 displayed a bi-modal expression pattern, showing an increase from E11.5 to E13.5 but decrease at E16.5 in varying degrees (sheet 2, 3, and 4 in Table S3 in Supporting Information). These proteins fell into the categories of "DNA replication", "mitochondrion organization", and "generation of precursor metabolites and energy", which implies that nucleotide and energy metabolism are more active during male PGC differentiation. Proteins in bi-modal expression patterns were also enriched in the process of "regulation of mitotic cell cycle", indicating that these proteins might be involved in mitotic arrest of male PGCs in E13.5. Altogether these observations indicate that after sex differentiation and entry into mitotic arrest, male PGCs actively provide proteins and metabolites to support the basic requirement for subsequent development and epigenetic modifications.

Comparison of protein expression profiles between female and male PGCs during sex differentiation

To identify the key proteins that potentially function in the sex-biased differentiation of PGCs, we further applied MA plot to analyze the DEPs between E11.5 and E13.5 PGCs in females and males, respectively (Tables S4 and S5 in Supporting Information). As shown in Figure 5A and B, the top 20 DEPs were labeled in each plot. Intriguingly, we found that some proteins, such as Ddx4, Ptbp2, Gcsh, Hdac2, Ssr1 and Pdlim1, were highly expressed in both female and male PGCs at E13.5 compared to E11.5, indicating that they are required for germ cell development but not differentiation. On the contrary, proteins such as Krt77, H3c7, and Mif were down-regulated in both female and male E13.5 PGCs, implying that these molecules are not essential for the subsequent development of PGCs after E11.5. Moreover, IPA (ingenuity pathway analysis) revealed that DEPs in the pathways related to DNA damage repair and protein degradation were highly divergent between E11.5 and E13.5 female PGCs, suggesting that they are likely to participate in the female PGC differentiation and onset of meiosis (Figure 5C). By contrast, DEPs between male E11.5 and E13.5 were enriched in pathways responsible for cleavage and polyadenylation of pre-mRNA and purine nucleotides *de novo* biosynthesis, indicating that these two molecular events are indispensable for male PGC differentiation and development (Figure 5D). It is worth noting that mitochondrial functions such as oxidative phosphorylation were required for both female and male PGC development during this period (Figure 5C and D).

In order to analyze how protein sets concordantly regulate the differentiation of PGCs, we used GSEA (gene set enrichment analysis) to obtain the GO annotation and enrich-

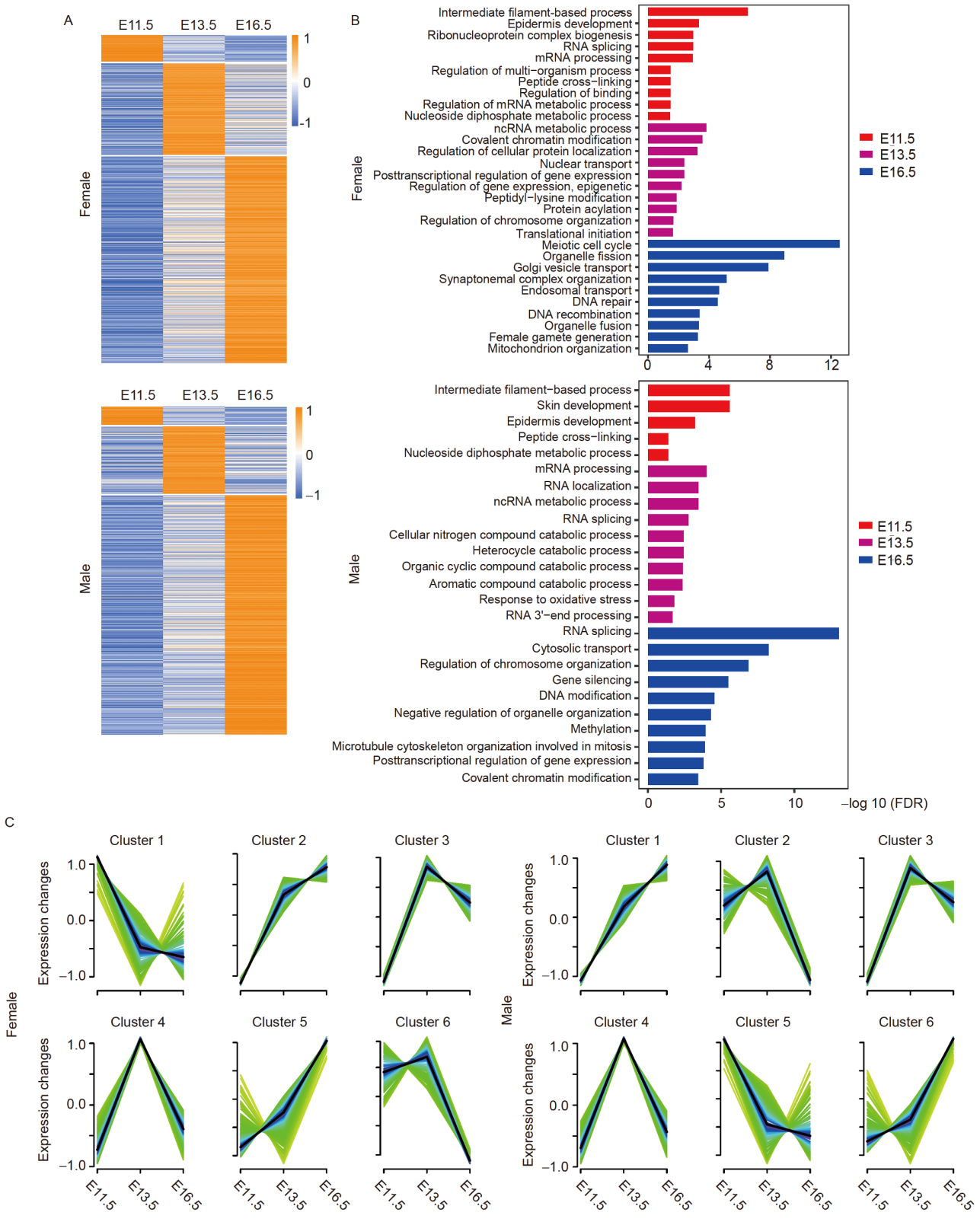

Figure 4 Proteomic analysis during female and male PGC development. A, Heatmap of DEPs showing the prominent divergence at different developmental stages in female and male PGCs. The color schema from blue to orange represents the relative abundance of proteins from low to high, respectively. Upper, female; lower, male. B, Functional annotation and GO (gene ontology) enrichment analysis of DEPs at different developmental stages in female and male PGCs by WebGestalt. The most enriched biological processes are showed based on significance value. The *x* axis represents –log10 transformed FDR (false discovery rate) value. Upper, female; lower, male. C, Clustering of distinct protein expression profiles in female and male PGCs from E11.5 to E16.5 by fuzzy c-means algorithm. Six clusters were summarized from female and male PGCs, respectively. The blue lines denote the major trend in each cluster. The *y* axis represents the normalized expression fold change in each stage. Left clusters, female; right clusters, male.

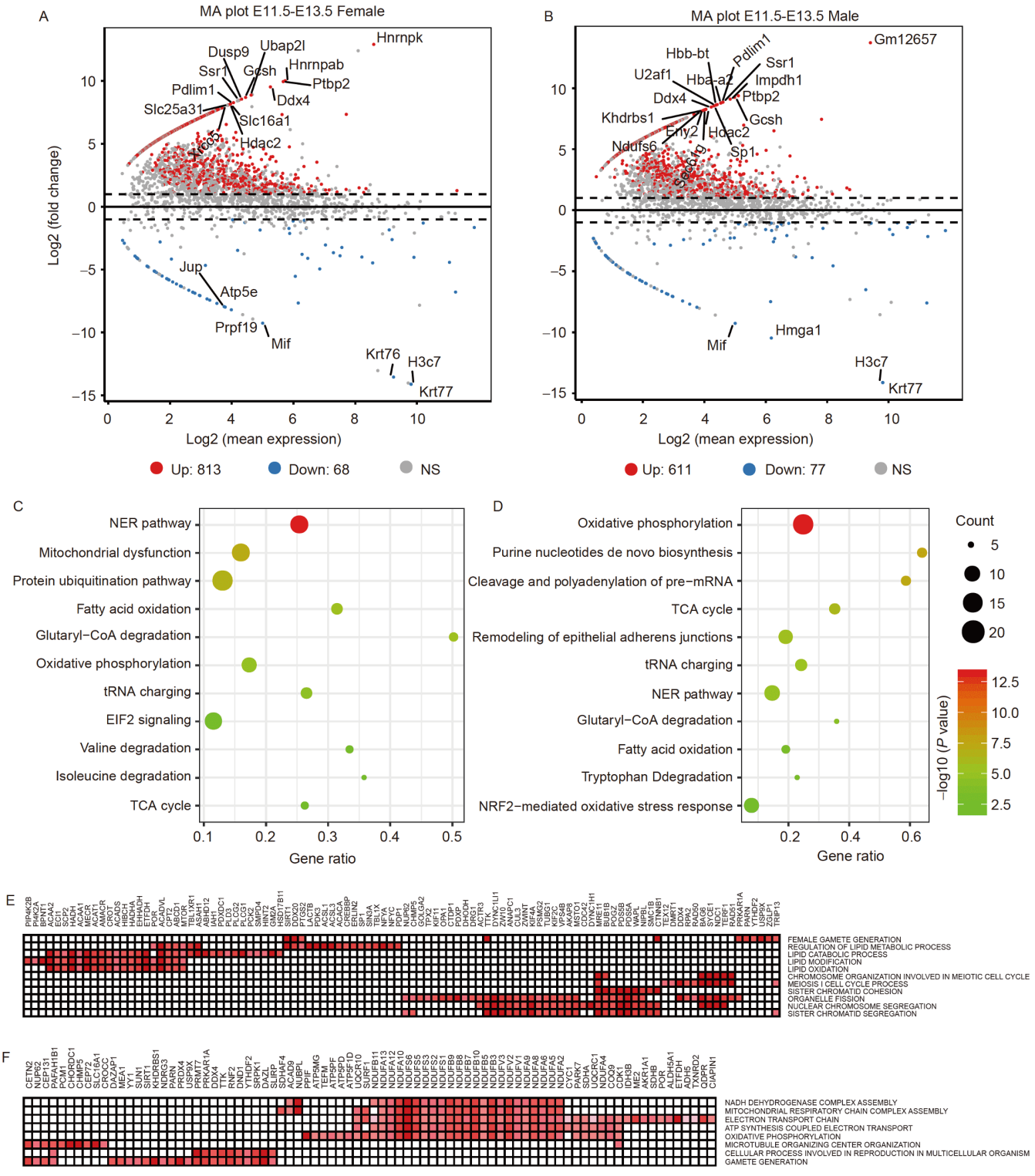

Figure 5 Proteomic comparison between female and male PGCs during sex differentiation. A and B, MA plot analysis of DEPs between E11.5 and E13.5 PGCs in females and males, respectively. The *x* axis and *y* axis respectively display log2 transformed mean expression of proteins and log2 transformed fold change, respectively. The red and blue plots denote proteins up- and down-regulated at E13.5 PGCs, respectively. Top 20 DEPs were labeled in each plot. C and D, IPA (ingenuity pathway analysis) showing the enriched pathways in female and male sex differentiation, respectively. Eleven representative pathways were included in each sex. Dot size indicates the count of overlapped proteins between the proteome dataset and pathways. The color key from green to red represents the overlapping significance from low to high. E and F, Leading edge analysis by GSEA to identify core proteins in enriched biological processes in female and male sex differentiation, respectively. One hundred and two proteins in 11 molecular events in females and 82 proteins in eight molecular events in males were identified. Color key from blue to red represents the protein expression level from low to high.

ment results. Through the comprehensive analysis of statistic enrichment score and *P*-value, we found that proteins were significantly enriched in the processes of chromosome segregation and lipid metabolism in E13.5 female PGCs compared to E11.5, indicating that the members of these protein sets had a synergistic effect during female PGC differentiation and meiosis initiation (Figure S4A in Supporting Information). The core proteins were extracted from these protein sets by the method of leading-edge analysis. Proteins such as Kif4a, Terf1, Pds5a, Pds5b, and Mre11 participate in cell cycle regulation and cytokinesis, while Acaa1, Acadvl, and Hadh are involved in lipid metabolic process (Figure 5E). By contrast, the processes such as "NADH dehydrogenase complex assembly", "Mitochondrial respiratory chain complex assembly", "ATP synthesis coupled electron transport" and "Oxidative phosphorylation" were active in E13.5 male PGCs compared to E11.5, demonstrating that energy metabolism is crucial for the male PGC differentiation. Reasonably, proteins in "cellular process involved in reproduction in multicellular organism" and "gamete generation" were also enriched in E13.5 male PGCs (Figure S4B in Supporting Information). By the leading-edge analysis, we further found that members in NADH: ubiquinone oxidoreductase protein family were simultaneously up-regulated to function in ATP synthesis and respiratory electron transport-related processes (Figure 5F).

Protein expression profile of female PGCs during meiosis

After E13.5, male PGCs enter into mitotic arrest, whereas female PGCs enter into the meiosis. We then employed MA plot to analyze the DEPs between E13.5 and E16.5 female PGCs to uncover the key regulatory pathways and molecules participating in the progress of meiosis. The plot result displayed that 404 proteins were up-regulated and 147 proteins were down-regulated from E13.5 to E16.5 female PGCs (Figure 6A; Table S6 in Supporting Information). Specifically, proteins implicated in the meiotic recombination such as Dmc1, Hormad1, Zcwpw1, Sycp1, and Sycp3 were present in the 20 top DEPs. The function analysis by IPA showed that most DEPs fell into categories "oogenesis", "formation of chiasmata", and "meiosis of female germ cells", confirming that female PGCs enter meiosis after E13.5 (Figure 6B). Also, we found that the biological processes related to meiotic recombination such as "homologous recombination", "repair of DNA", and "double-stranded DNA break repair" were activated in E16.5 female PGCs (Figure 6B). These results were further verified by the IPA activation function submodule (*z*-score≥2), displaying that DEPs were highly enriched to activate functions of "development of reproductive system" and "gametogenesis" when female PGCs developed from E13.5 to E16.5 (Figure 6C).

Interestingly, we also discovered that DNA damage response signaling pathways such as "ATM signaling" and "roles of CHK proteins in cell cycle checkpoint control" were activated in E16.5 female PGCs as assessed by IPA of canonical pathway (Figure 6D). Expansion of these two pathways provided an elaborated view of the proteins taking part in the related molecular functions (Figure S5A and B in Supporting Information). We further performed the leading-edge analysis by GSEA to identify the proteins that play critical roles in the GO terms related to meiosis and recombination in E16.5 female PGCs. The heatmap showed that every molecular event required a group of proteins to coordinately exert functions. For example, Dcaf1, Xrcc4, Mcm8, Mre11, Atm, Sycp1, Dmc1, and Mlh1 were simultaneously up-regulated in GO term "DNA recombination" (Figure 6E). Thus, these data provided a comprehensive view regarding which combination of proteins is essential for the meiotic events from E13.5 to E16.5 female PGCs.

DNA damage response pathway is required for female PGC development

Since proteins in DNA damage response signaling pathways were found up-regulated in E16.5 female PGCs, we verified their functions in meiosis using a fetal ovary culture system with the inhibitor of ATR, an apical regulator of the response to DNA damage (Matsuoka et al., 2007; Shiloh, 2001). ATR has been proved to be a crucial regulator of meiotic prophase progression in male mice, while the function of ATR in prophase I progression of oocyte has not been elucidated in detail (Pacheco et al., 2018; Widger et al., 2018). To this end, fetal ovaries were cultured *in vitro* and the chromosomes of PGCs were released under the hypotonic condition. Immunofluorescence microscopy was used to obtain images of the chromosome spreads. Nuclei were stained with antibodies against Sycp1 and Sycp3 on the chromosomes. Consistent with previous results (Zhou et al., 2018), in control female PGCs at prophase I, we observed that Sycp3 appeared during the leptonema and remained on the chromosome axis until pachynema. Sycp1, a central element (CE) component, was not observed during the leptonema but appeared at the zygonema. The full-length synaptonemal complex (SC) assembled completely at the pachynema (Figure 7A). In striking contrast, when fetal female gonad was treated with ATR inhibitor AZ20, the synapsis organization was partially disrupted at pachynema and the proportions of nuclei at different substages of meiotic prophase I were altered compared to the controls (Figure 7A). In addition, we found that γH2AX foci, the marker of DSB formation, accumulated at leptonema and disappeared at pachynema in the control germ cells. However, they were still present at pachynema in ATR-inhibited cells, indicating

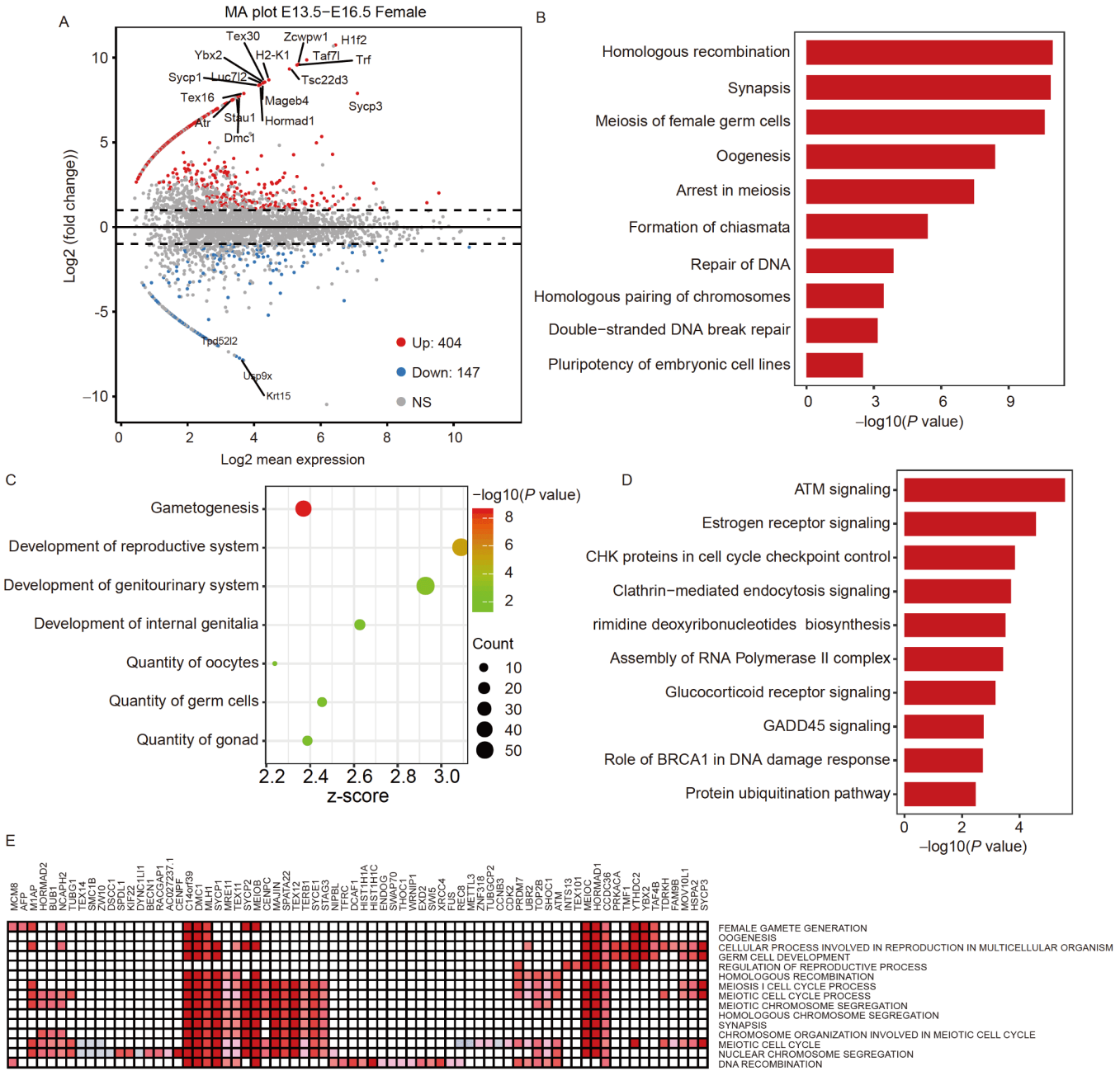

Figure 6 Proteomic analysis of female PGC during meiosis. A, MA plot analysis of DEPs between E13.5 and E16.5 female PGCs during meiosis. The *x* axis and *y* axis display log2 transformed mean expression of proteins and log2 transformed fold change, respectively. The red and blue plots represent proteins up- and down-regulated at E13.5PGCs, respectively. Top 20 DEPs were labeled in each plot. B and D, IPA showing the enriched functions and canonical pathway in meiosis of female PGCs. Ten representative functions and pathways were included in each analysis. The *x* axis of the bar chart represents –log10 transformed *P*-value, equal to the bar width. C, IPA showing activation function submodule in meiosis of female PGCs. Dot size indicates the count of overlapped proteins between the proteome dataset and functions. Color key from green to red represents overlapping significance from low to high. The corresponding quantitative values were –log10 transformed *P* values. E, Leading edge analysis by GSEA to identify the proteins involved in meiosis and recombination processes in E16.5 female PGCs. Seventy-two proteins were identified from 15 molecular events. Color key from blue to red represents the protein expression level from low to high.

that DSBs were not properly repaired when DNA damage response pathway was blocked (Figure 7B). This observation was further confirmed by the staining of Rad51, a core recombinase for homologous recombination repair of DSBs (Sung et al., 2003). Rad51 foci were not detectable at pachynema in controls but persisted on the chromosomes in ATR-inhibited germ cells. Accordingly, the number of Rad51 foci remained higher in ATR-inhibited cells than that in controls at pachynema (Figure 7C). Altogether, these data indicate that DNA damage response pathway is essential for meiotic recombination and progression.

To investigate the consequence of the defects in meiosis

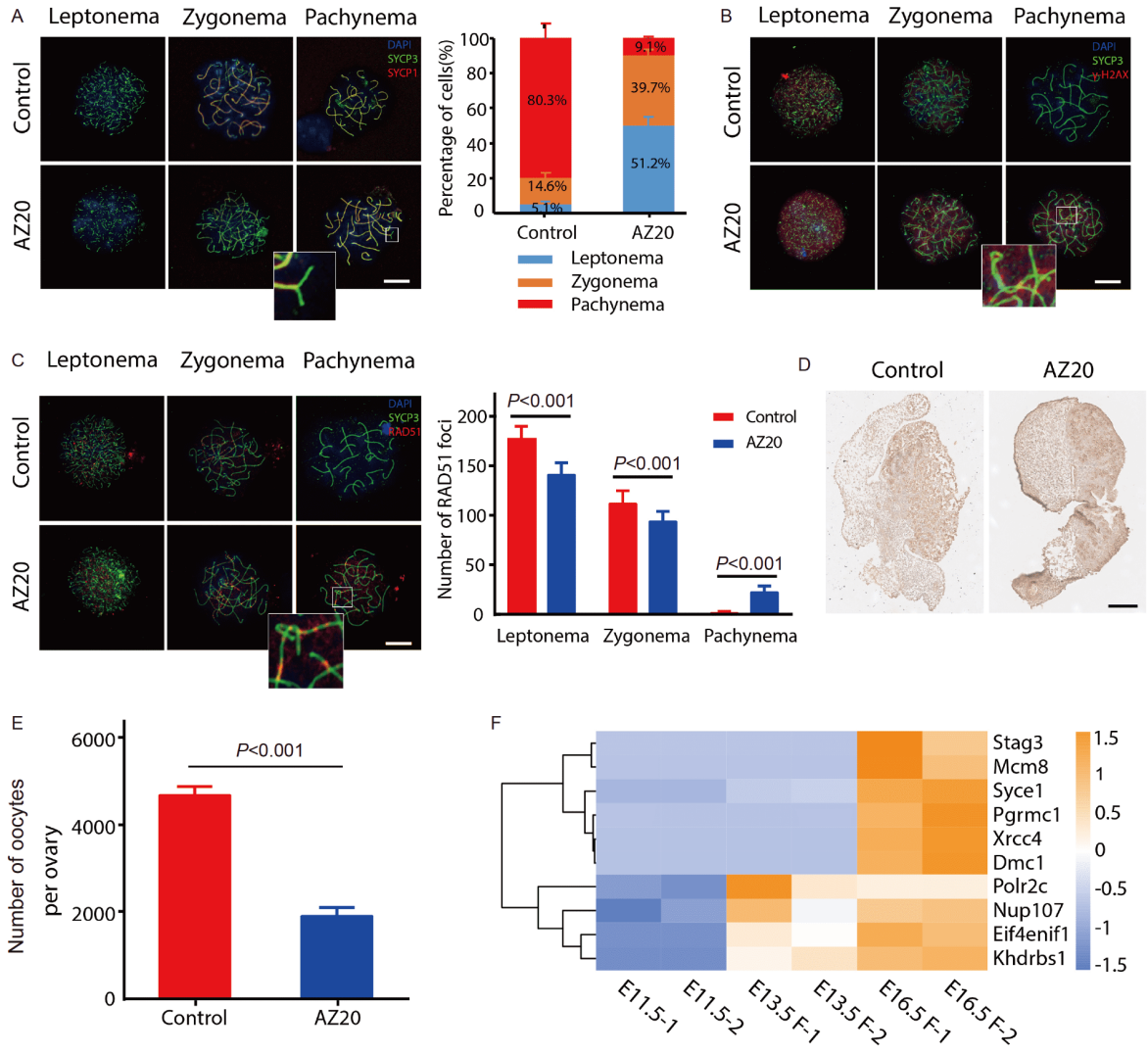

Figure 7 DNA damage response factor ATR is required for female PGC development. A, Chromosome spreads of female meiotic PGCs treated with or without ATR inhibitor AZ20. Fetal ovaries were cultured *in vitro* with or without 5 μmol L^{-1} AZ20 for 3 days followed by meiotic chromosome spreading of PGCs. Chromosome spreads were labeled by Sycp1 and Sycp3. Scale bar, 10 μm. The percentage of different sub-stages of E16.5 PGCs was summarized in the histogram. At least 200 PGCs from three fetal ovaries were included in each group. Error bars represent the standard deviation. B, DNA damage staining of chromosome spreads of female meiotic PGCs treated with or without ATR inhibitor AZ20. The chromosome spreads were co-stained with Sycp3 and DNA double-strand break marker γH2AX. Scale bar, 10 μm. C, Rad51 staining of chromosome spreads of female meiotic PGCs treated with or without ATR inhibitor AZ20. The chromosome spreads were co-stained with Sycp3 and DNA repair core recombinase Rad51. The foci number of Rad51 in individual cells from each group was calculated and summarized in the histogram. At least 30 cells were included for each group. Error bars represent the standard deviation. Scale bar, 10 μm. D, Immunohistochemical staining of female germ cells in genital ridges treated with or without ATR inhibitor AZ20. E13.5 fetal ovaries were cultured for 3 days *in vitro* with or without 5 μmol L^{-1} AZ20 followed by section and staining of germ cell marker Vasa. Scale bar, 100 μm. E, The numbers of germ cells in E16.5 fetal ovaries treated with or without ATR inhibitor AZ20 were counted and summarized. At least three fetal ovaries were included for each group. Error bars represent the standard deviation. F, The heatmap of reported POI genes in full process of female PGC development. Color key from blue to orange represents the protein expression level from low to high.

resulting from the inhibition of DNA damage response pathway, we tested the status of female germ cells in genital ridge. E13.5 fetal ovaries were cultured for 3 days *in vitro* followed by immunohistochemical staining of germ cell marker Vasa. Vasa-positive signals were abundantly and evenly distributed in the control fetal ovaries, whereas prominently lost in ATR-inhibited fetal ovaries (Figure 7D and E), implying that DSB repair is indispensable for the survival of female germ cells. Lastly, we found that the reported pathogenic genes of POI (primary ovarian insufficiency) (Jiao et al., 2018; Katari et al., 2018) are up-regulated at E16.5 female PGCs, and these genes are related to DNA damage repair, homologous recombination and meiosis (Figure 7F), indicating that the DNA repair mechanisms are intensively involved in the development of germ cells.

DISCUSSION

PGCs are highly specialized cells that generate gametes

through meiosis to transmit genetic and epigenetic traits between generations (Hill et al., 2018; Strome and Updike, 2015). It has been reported that PGCs are induced from a subset of cells in peri-implantation epiblast by BMP signaling from the surrounding tissues in mammals, and then initiate a unique developmental program that involves comprehensive epigenetic resetting and repression of somatic genes to promote germ cell identity (Sybirna et al., 2019). Recent studies have comprehensively analyzed the transcriptome, methylome, and chromatin accessibility profiles of PGCs in both mice and humans, revealing a complicated mechanism regulating the dynamics of gene expression, epigenetic reprogramming, and chromatin state during PGC development (Guo et al., 2015; Guo et al., 2017; Seisenberger et al., 2012; Yamaguchi et al., 2013). However, as the final executor of the biological functions in the cell, protein expression patterns during PGC differentiation and development are largely unknown, although a proteome profile of female mouse gonads from E11.5 to E13.5 has been mapped (Shen et al., 2018).

In current work, we systematically constructed a spatial map and comparative proteome profiles of female and male PGCs at E11.5, E13.5 and E16.5, spanning the critical windows for sex-biased differentiation, male mitotic arrest and female meiosis initiation in PGCs. At the beginning of colonization in genital ridge, there are around 3,500 PGCs in 1,300 nests at E11.5. Both female and male PGCs undergo an obvious proliferation within their located nests from E11.5 to E13.5. Of note, the number of nests during this period keeps constant while the volume dramatically grows. This demonstrates that in their initial development in the genital ridge, a special microenvironment by cellular interaction in the nest is required for PGCs' proliferation. To form single germ cells for fertilization in the future, PGCs should separate each other finally. Thus, the nests fragment from E13.6 to E16.5.

In general, we detected around 2,000–3,000 proteins at each developmental time-point in both male and female PGCs. Interestingly, E11.5 PGCs showed much different protein expression profiles from E13.5 and E16.5, which is consistent with the previous notion that sex differentiation is established between E11.5 and E13.5 (Brennan and Capel, 2004; Yokobayashi et al., 2013). In addition, when comparing the profiles in male PGCs with the female at the same developmental stage in parallel, they did not show the big discrepancy at E13.5, but did at E16.5, suggesting that PGCs start to express sex-biased unique proteins for their subsequent development after differentiation. Notably, the comparative analysis of proteomic and transcriptomic profiling shows the poor correlation between protein expression and RNA expression during PGC development, which highlights the importance and the value of proteomic data. The poor correlation may result from expression delay between mRNA and protein or even unknown reasons for future investigation.

Another intriguing finding in our study is that pathways related to mitochondrial functions participated in the PGC differentiation. This is concordant with a recent proteomic study in the female mouse fetal gonads showing that the electron transport chain of mitochondria plays an important role in female development (Shen et al., 2018). Similarly, energy metabolism pathways such as TCA cycle and oxidative phosphorylation were found active during male PGC differentiation and mitotic arrest, which is consistent with a previous report indicating that oxidative phosphorylation is necessary for the control of PGC reprogramming and specification of pluripotent stem cells into PGCs in culture (Hayashi et al., 2017). In addition, when female PGCs enter meiosis after E13.5, proteins implicated in the DNA damage repair and meiotic recombination were simultaneously upregulated to coordinately exert functions, implying that they are the most essential molecular events that occur at the early stage of female meiosis. Lastly, we verified that the function of ATR, a pivotal governor in DNA damage response pathway, is critical for meiotic recombination, progression, and survival for female PGCs. Therefore, the proteomic profiles may provide insights into the genetic etiology of gametogenesis defects and infertility. In summary, our findings demonstrate that the proteome landscape of mouse PGCs is in general distinct from the transcriptome, thereby providing a reliable resource for the mechanistic studies of the core players and regulators during PGC differentiation and development.

MATERIALS AND METHODS

Animals and sample collection

Genital ridges and fetal gonads were obtained from female C57BL/6 mice crossed with male homozygous Oct4-GFP transgenic mice (Jackson Lab). Noon on the day of vaginal plug observed was defined as E0.5. Genital ridges were isolated from E11.5 embryos, while from E13.5 female and male fetal gonads were collected separately by the distinguished morphology. The gonads were dispersed into cell suspensions by Accutase digestion with shaking at 500 r min^{-1} for 30 min at 37°C. The suspensions were then filtered through a 40 μm strainer to obtain single cell suspensions for flow cytometry (FACS Aria II SORP, BD Bioscience). GFP-positive PGCs were sorted. The sorted PGCs were further washed with DPBS and stored at –80°C. The sorted cells were further identified by immunostaining for germ cell marker Vasa.

Chemicals and antibodies

All chemicals were purchased from Sigma except for those

specifically mentioned. Anti-Sycp3 (ab97672), Sycp1 (ab15090), and Rad51 (ab63801) antibodies were purchased from Abcam. Anti-γH2AX (2577S) antibody was purchased from Cell Signaling Technology. Anti-VASA (51042-1-AP) and GATA4 (19530-1-AP) antibodies were purchased from Proteintech. Alexa Fluor 488 goat anti-mouse (A-28175) and Alexa Fluor 555 goat anti-rabbit (A-21428) were purchased from Thermo Fisher Scientific. AZ20 (S7050) was purchased from Selleck. BD Cytofix (554655) was purchased from BD Biosciences. Millicell Cell Culture Insert (PICM0RG50) was purchased from Millipore.

Volume staining of intact genital ridge

Intact genital ridge immunostaining was performed according to the previous protocol (Li et al., 2019). Briefly, genital ridges were surgically isolated from pregnant mice and fixed overnight in BD Cytofix on a shaker at 4°C. Fixed genital ridges were washed three times for 1 h with washing buffer (1× PBS supplemented with 0.3% Triton X-100 and 0.5% 1-thioglycerol). After that, the genital ridges were blocked and permeabilized for 24 h in blocking buffer (1× PBS supplemented with 0.3% Triton X-100, 1% BSA, and 1% normal mouse serum) at 37°C on the shaker. The tissues were incubated with the primary antibody of GATA4 (1:200) for one week at room temperature and washed for 12 h at 37°C. Then the tissues were immerged in fresh washing buffer which was changed every 12 h for three times at room temperature. Genital ridges were subsequently incubated with fluorescently labeled secondary antibody (1:400) and hochest33342 (10 μg mL^{-1}) for one week at room temperature. After washing for three times, genital ridges were immerged in clearing solution (2.75 mL of 40% N-methyl acetamide, 4 g of Histodenz, and 5 μL Triton X-100) with a refractive index of 1.475–1.505, for 24 h at room temperature. The cleared samples were used for subsequent 3D imaging and modeling.

Genital ridges 3D modeling

Images of genital ridges immersing in clearing solution were acquired by Lightsheet Z.1 microscope with a 20× detection objective (NA=1.0 Corr nd=1.48). The images were treated with dual side fusion and converted to Imaris file format with Imaris File Converter. The multiview image tiles were stitched with precise alignment by Imaris stitcher software. Then the fused images were imported into Imaris program for 3D visualization and analysis. The 3D surface rendering of Oct-4-GFP and GATA4 (555 channel) was carried out to obtain a 3D reconstruction of PGCs and genital ridges. The volume of genital ridges was calculated by virtue of the GATA4 channel surface creation. Quantitative analysis of PGC clusters (nests) was performed by Spots module of Imaris.

Protein extraction and digestion

PGC samples were lysed with 400 μL lysis buffer (20 mmol L^{-1} HEPES, 10 mmol L^{-1} KCL, 1.5 mmol L^{-1} $MgCl_2$, 10 mmol L^{-1} DTT, pH 7.4) on ice for 30 min. The supernatant was collected by centrifugation at 10,000×*g* for 2 min at 4°C and then concentrated by 10 kD ultrafiltration spin columns. Proteins were then maintained in 50 μL 50 mmol L^{-1} NH_4HCO_3 and digested with trypsin at 37°C for 16 h. Digested peptides were collected through centrifugation (14,000×*g* for 20 min at 4°C) and then desalinated by C18 desalination columns. Samples were eluted with 80 μL elution buffer (50% acetonitrile, 0.1% formic acid) and the solutions were dried to less than 50 μL through a vacuum centrifugation dryer at 45°C, 1,500 r min^{-1}.

LC-MS/MS analysis

Digested peptide mixtures were analyzed on an Orbitrap Fusion Lumos (Thermo Fisher Scientific) mass spectrometer interfaced with an Easy-nLC 1200 nanoflow liquid chromatography system (Thermo Fisher Scientific) with a Nono Spray ionization (NSI) in positive ion polarity. Samples were dissolved with 12 μL of Solvent A (0.1% formic acid in water), and 5 μL was loaded to a homemade trap column (100 μm×2 cm) packed with C18 reverse-phase resin (particle size, 3 μm; pore size, 120 Å; SunChrom, USA) at a maximum pressure of 220 bar with 12 μL of solvent A, then separated on a 150 μm×12 cm silica microcolumn (homemade, particle size, 1.9 μm; pore size, 120 Å; SunChrom, USA) with a gradient of 10%–37% mobile phase B (80% acetonitrile and 0.1% formic acid) at a flow rate of 600 nL min^{-1} for 60 min. The gradient elution conditions (60 min) were: 10% to 13% mobile phase B for 3 min; 13% to 29% for 39 min; 29% to 37% for 11 min; 37% to 95% for 1 min; 95% for 6 min. The MS analysis was performed in a data-dependent manner (DDA) with full scans (*m*/*z* 350–1,500) acquired using an Orbitrap mass analyzer at a mass resolution of 120,000. The most intense ions selected under top-speed mode were isolated in Quadrupole with a 1.6 *m*/*z* window and fragmented by higher energy collisional dissociation (HCD) with a normalized collision energy of 32%, then detected in the Orbitrap at a mass resolution of 15,000. The automatic gain control (AGC Targets) for full MS was set to 4e5, and that for MS/MS was set to 5e4, with maximum ion injection times of 50 and 22 ms, respectively. The dynamic exclusion time was 30 s.

Bioinformatics data interpretation

Raw files were searched against the mouse RefSeq protein database (2017/11/01) with Proteome Discoverer (Thermo Fisher Scientific, version 2.1) using the SEQUEST HT

search engine with percolator. The mass tolerance of the precursor ions was set to 20 ppm. The tolerance of the product ions was set to 0.06 Da. Up to two missed cleavages were allowed for trypsin digestion. Carbamidomethylation of cysteine, N-terminal protein acetylation, and methionine oxidation were set as variable modifications. The data were also searched against a decoy database so that protein identifications were accepted at a false discovery rate of 1%. Protein quantifications were measured using a label-free, T3PQ (Top 3 protein quantification) approach. For batch-to-batch comparison, the quantifications were converted into FOT (fraction of total) representing a normalized abundance. For visualization purpose, the number of FOT is multiplied by 10^5.

Bioinformatics analysis

Heat maps of the protein expression profiles were generated using R packages. t-SNE, principal components analysis (PCA) and hierarchical clustering analysis were conducted in NetworkAnalyst (https://www.networkanalyst.ca/). Pathway enrichment and GO analysis were conducted using the Web-based GEne SeT AnaLysis Toolkit (WebGestalt, http://www.webgestalt.org/), and *P*-values for the representative GO terms shown in the present study were adjusted with the Benjamini-Hochberg procedure (Liao et al., 2019). MinDet (deterministic minimum imputation) method was adopted to conduct the imputation of missing values, NA values were substituted by number "0.1". Proteins from three developmental stages were grouped into different clusters using Mfuzz package in R with fuzzy c-means algorithm (Kumar and M, 2007). Correlation analysis of mRNA and protein expression between different developmental stages was carried out in common genes using Pearson's correlation. MA plot was conducted for visual representation of differential expressed proteins between two stages by R packages. Gene set enrichment analysis (GSEA, http://software.broadinstitute.org/gsea/index.jsp) was conducted to identify concordant differences between two stages, and then the enrichment results were analyzed by Leading Edge Analysis to get the core enriched proteins (Subramanian et al., 2005). Gene expression signatures of different developmental stages were analyzed by Ingenuity® Pathway Analysis (https://www.qiagenbioinformatics.com/products/ingenuity-pathway-analysis/), according to the instructions provided. Active pathway was defined when *z*-score 2 (Krämer et al., 2014).

Fetal ovary culture and chromosome spreading

Fetal ovaries attached with mesonephros were isolated at E13.5, and cultured on the 0.4 μm inserts in a 6-well plate. Samples were incubated with 5% CO_2 at 37°C in culture medium DMEM/F-12 supplemented with 1% penicillin-streptomycin and 1× ITS initially, and then treated with 5 μmol L^{-1} AZ20. The equivalent volume of DMSO was added to the control medium. After cultured for 3 days *in vitro*, fetal ovaries were removed and incubated in a 4-well plate containing hypotonic extraction buffer (30 mmol L^{-1} Tris-Cl, 50 mmol L^{-1} sucrose, 17 mmol L^{-1} trisodium citrate dihydrate, 5 mmol L^{-1} EDTA, 0.5 mmol L^{-1} DTT, 0.1 mmol L^{-1} PMSF, pH 8.2) for 30 min. The ovaries were punctured to release germ cells in 40 μL 100 mmol L^{-1} sucrose solution on a glass slide. Then the cell suspensions were dissociated by gentle pipetting and pipetted into fixative droplet (1% PFA, 0.15% Triton X-100, pH 9.2) on a slide. The cell suspensions were spread to cover the slide and then fixed and dried for 2 h in a humidified box. The slides were washed twice for 5 min in 0.4% Photo-Flo and air-dried. For immunofluorescence staining, the chromosome spread slides were incubated with the indicated primary antibodies overnight at 4°C. After washing three times, the slides were incubated with secondary antibodies for 1 h at room temperature and stained with Hoechst33342 for 5 min. Fluorescence analysis of chromosomes was conducted by a confocal laser scanning microscope at 63×/1.40 (Carl Zeiss 710).

Immunohistochemistry (IHC)

Fetal ovaries that were cultured *in vitro* for 3 days were removed and fixed in 4% paraformaldehyde for 24 h, dehydrated in gradient alcohol, and paraffin-embedded. Paraffin blocks were cut into 5 μm serial sections followed by antigen retrieval. Endogenous peroxidase was eliminated with 3% hydrogen peroxide at room temperature for 10 min. Sections were incubated with anti-Vasa (1:200) antibody and detected with Dako Envision System, followed by dehydration and mounting. Images were taken and analyzed by NanoZoomer SQ and NDP view 2.6.8 system. The germ cell counting was conducted with Image J software.

Statistical analysis

Student's *t*-tests were performed using GraphPad Prism software, and data were presented as means±SEM. The statistical differences were considered significant when the *P*-value <0.05.

Data availability

The mass spectrometry proteomics data have been deposited to the ProteomeXchange Consortium (http://proteomecentral.proteomexchange.org) via the iProX partner repository with the dataset identifier PXD019222.

Compliance and ethics *The author(s) declare that they have no conflict of interest. The institutional and national guide for the care and use of laboratory animals was followed.*

Acknowledgements *This work was supported by the National Key Research and Development Program of China (2017YFC1001501, 2016YFC1000604, 2018YFC1004002) and the Foundation for Innovative Research Groups of National Natural Science Foundation of China (81521002).*

References

Agarwal, A., Mulgund, A., Hamada, A., and Chyatte, M.R. (2015). A unique view on male infertility around the globe. Reprod Biol Endocrinol 13, 37.

Bhattacharyya, T., Walker, M., Powers, N.R., Brunton, C., Fine, A.D., Petkov, P.M., and Handel, M.A. (2019). Prdm9 and meiotic cohesin proteins cooperatively promote DNA double-strand break formation in mammalian spermatocytes. Curr Biol 29, 1002–1018.e7.

Brennan, J., and Capel, B. (2004). One tissue, two fates: molecular genetic events that underlie testis versus ovary development. Nat Rev Genet 5, 509–521.

Ewen, K.A., and Koopman, P. (2010). Mouse germ cell development: from specification to sex determination. Mol Cell Endocrinol 323, 76–93.

Gkountela, S., Li, Z., Vincent, J.J., Zhang, K.X., Chen, A., Pellegrini, M., and Clark, A.T. (2013). The ontogeny of cKIT+ human primordial germ cells proves to be a resource for human germ line reprogramming, imprint erasure and *in vitro* differentiation. Nat Cell Biol 15, 113–122.

Godin, I., Wylie, C., and Heasman, J. (1990). Genital ridges exert long-range effects on mouse primordial germ cell numbers and direction of migration in culture. Development 108, 357–363.

Guo, F., Yan, L., Guo, H., Li, L., Hu, B., Zhao, Y., Yong, J., Hu, Y., Wang, X., Wei, Y., et al. (2015). The transcriptome and DNA methylome landscapes of human primordial germ cells. Cell 161, 1437–1452.

Guo, H., Hu, B., Yan, L., Yong, J., Wu, Y., Gao, Y., Guo, F., Hou, Y., Fan, X., Dong, J., et al. (2017). DNA methylation and chromatin accessibility profiling of mouse and human fetal germ cells. Cell Res 27, 165–183.

Hayashi, K., de Sousa Lopes, S.M.C., and Surani, M.A. (2007). Germ cell specification in mice. Science 316, 394–396.

Hayashi, Y., Otsuka, K., Ebina, M., Igarashi, K., Takehara, A., Matsumoto, M., Kanai, A., Igarashi, K., Soga, T., and Matsui, Y. (2017). Distinct requirements for energy metabolism in mouse primordial germ cells and their reprogramming to embryonic germ cells. Proc Natl Acad Sci USA 114, 8289–8294.

Hikabe, O., Hamazaki, N., Nagamatsu, G., Obata, Y., Hirao, Y., Hamada, N., Shimamoto, S., Imamura, T., Nakashima, K., Saitou, M., et al. (2016). Reconstitution *in vitro* of the entire cycle of the mouse female germ line. Nature 539, 299–303.

Hill, P.W.S., Leitch, H.G., Requena, C.E., Sun, Z., Amouroux, R., Roman-Trufero, M., Borkowska, M., Terragni, J., Vaisvila, R., Linnett, S., et al. (2018). Epigenetic reprogramming enables the transition from primordial germ cell to gonocyte. Nature 555, 392–396.

Jameson, S.A., Natarajan, A., Cool, J., DeFalco, T., Maatouk, D.M., Mork, L., Munger, S.C., and Capel, B. (2012). Temporal transcriptional profiling of somatic and germ cells reveals biased lineage priming of sexual fate in the fetal mouse gonad. PLoS Genet 8, e1002575.

Jiao, X., Ke, H., Qin, Y., and Chen, Z.J. (2018). Molecular genetics of premature ovarian insufficiency. Trends Endocrinol Metab 29, 795–807.

Katari, S., Aarabi, M., Kintigh, A., Mann, S., Yatsenko, S.A., Sanfilippo, J. S., Zeleznik, A.J., and Rajkovic, A. (2018). Chromosomal instability in women with primary ovarian insufficiency. Human Reprod 33, 531–538.

Krämer, A., Green, J., Pollard Jr, J., and Tugendreich, S. (2014). Causal analysis approaches in Ingenuity Pathway Analysis. Bioinformatics 30, 523–530.

Kumar, L., and E Futschik, M. (2007). Mfuzz: a software package for soft clustering of microarray data. Bioinformation 2, 5–7.

Lei, L., and Spradling, A.C. (2013). Mouse primordial germ cells produce cysts that partially fragment prior to meiosis. Development 140, 2075–2081.

Li, W., Germain, R.N., and Gerner, M.Y. (2019). High-dimensional cell-level analysis of tissues with Ce3D multiplex volume imaging. Nat Protoc 14, 1708–1733.

Liao, Y., Wang, J., Jaehnig, E.J., Shi, Z., and Zhang, B. (2019). WebGestalt 2019: gene set analysis toolkit with revamped UIs and APIs. Nucleic Acids Res 47, W199–W205.

Lin, Y., Gill, M.E., Koubova, J., and Page, D.C. (2008). Germ cell-intrinsic and -extrinsic factors govern meiotic initiation in mouse embryos. Science 322, 1685–1687.

Martínez-Arroyo, A.M., Medrano, J.V., Remohí, J., and Simón, C. (2014). Germ line development: lessons learned from pluripotent stem cells. Curr Opin Genet Dev 28, 64–70.

Matsuoka, S., Ballif, B.A., Smogorzewska, A., McDonald, E.R., Hurov, K. E., Luo, J., Bakalarski, C.E., Zhao, Z., Solimini, N., Lerenthal, Y., et al. (2007). ATM and ATR substrate analysis reveals extensive protein networks responsive to DNA damage. Science 316, 1160–1166.

Pacheco, S., Maldonado-Linares, A., Marcet-Ortega, M., Rojas, C., Martínez-Marchal, A., Fuentes-Lazaro, J., Lange, J., Jasin, M., Keeney, S., Fernández-Capetillo, O., et al. (2018). ATR is required to complete meiotic recombination in mice. Nat Commun 9, 2622.

Paigen, K., and Petkov, P. (2010). Mammalian recombination hot spots: properties, control and evolution. Nat Rev Genet 11, 221–233.

Pepling, M.E., and Spradling, A.C. (2001). Mouse ovarian germ cell cysts undergo programmed breakdown to form primordial follicles. Dev Biol 234, 339–351.

Sabour, D., Araúzo-Bravo, M.J., Hübner, K., Ko, K., Greber, B., Gentile, L., Stehling, M., and Schöler, H.R. (2011). Identification of genes specific to mouse primordial germ cells through dynamic global gene expression. Hum Mol Genet 20, 115–125.

Saitou, M., and Yamaji, M. (2010). Germ cell specification in mice: signaling, transcription regulation, and epigenetic consequences. REPRODUCTION 139, 931–942.

Saitou, M., and Yamaji, M. (2012). Primordial germ cells in mice. Cold Spring Harb Perspect Biol 4, a008375.

Seisenberger, S., Andrews, S., Krueger, F., Arand, J., Walter, J., Santos, F., Popp, C., Thienpont, B., Dean, W., and Reik, W. (2012). The dynamics of genome-wide DNA methylation reprogramming in mouse primordial germ cells. Mol Cell 48, 849–862.

Shen, C., Li, M., Zhang, P., Guo, Y., Zhang, H., Zheng, B., Teng, H., Zhou, T., Guo, X., and Huo, R. (2018). A comparative proteome profile of female mouse gonads suggests a tight link between the electron transport chain and meiosis initiation. Mol Cell Proteomics 17, 31–42.

Shiloh, Y. (2001). ATM and ATR: networking cellular responses to DNA damage. Curr Opin Genet Dev 11, 71–77.

Strome, S., and Updike, D. (2015). Specifying and protecting germ cell fate. Nat Rev Mol Cell Biol 16, 406–416.

Subramanian, A., Tamayo, P., Mootha, V.K., Mukherjee, S., Ebert, B.L., Gillette, M.A., Paulovich, A., Pomeroy, S.L., Golub, T.R., Land er, E.S., et al. (2005). Gene set enrichment analysis: a knowledge-based approach for interpreting genome-wide expression profiles. Proc Natl Acad Sci USA 102, 15545–15550.

Sung, P., Krejci, L., Van Komen, S., and Sehorn, M.G. (2003). Rad51 recombinase and recombination mediators. J Biol Chem 278, 42729–42732.

Sybirna, A., Wong, F.C.K., and Surani, M.A. (2019). Genetic basis for primordial germ cells specification in mouse and human: Conserved and divergent roles of PRDM and SOX transcription factors. Curr Top Dev Biol 135, 35–89.

Tam, P.P., and Snow, M.H. (1981). Proliferation and migration of primordial germ cells during compensatory growth in mouse embryos. J Embryol Exp Morphol 64, 133–147.

Tan, H., and Tee, W.W. (2019). Committing the primordial germ cell: An

updated molecular perspective. WIREs Syst Biol Med 11, e1436.
Wen, L., Liu, Q., Xu, J., Liu, X., Shi, C., Yang, Z., Zhang, Y., Xu, H., Liu, J., Yang, H., et al. (2020). Recent advances in mammalian reproductive biology. Sci China Life Sci 63, 18–58.
Widger, A., Mahadevaiah, S.K., Lange, J., ElInati, E., Zohren, J., Hirota, T., Pacheco, S., Maldonado-Linares, A., Stanzione, M., Ojarikre, O., et al. (2018). ATR is a multifunctional regulator of male mouse meiosis. Nat Commun 9, 2621.
Yamaguchi, S., Hong, K., Liu, R., Inoue, A., Shen, L., Zhang, K., and Zhang, Y. (2013). Dynamics of 5-methylcytosine and 5-hydroxymethylcytosine during germ cell reprogramming. Cell Res 23, 329–339.
Yokobayashi, S., Liang, C.Y., Kohler, H., Nestorov, P., Liu, Z., Vidal, M., van Lohuizen, M., Roloff, T.C., and Peters, A.H.F.M. (2013). PRC1 coordinates timing of sexual differentiation of female primordial germ cells. Nature 495, 236–240.
Zhou, Z., Wang, L., Ge, F., Gong, P., Wang, H., Wang, F., Chen, L., and Liu, L. (2018). *Pold3* is required for genomic stability and telomere integrity in embryonic stem cells and meiosis. Nucleic Acids Res 46, 3468–3486.

SUPPORTING INFORMATION

The supporting information is available online at https://doi.org/10.1007/s11427-020-1762-2. The supporting materials are published as submitted, without typesetting or editing. The responsibility for scientific accuracy and content remains entirely with the authors.